



Flow Characteristics of Cylinders with Asymmetric Grooves: A Modeling and Experimental Study

F. Yan¹, W. Kong¹, H. Jiao^{2,3}, F. Peng¹ and J. Zhang^{1,†}

¹ School of Mechanical Engineering, Jiangsu University of Science and Technology, Zhenjiang 212000, China

² China ship Scientific Research Center, Wuxi 214082, China

³ Taihu Laboratory of Deepsea Technological Science, Wuxi 214082, China

[†]Corresponding Author Email: zhjian127@just.edu.cn

ABSTRACT

This study examined the drag reduction properties of cylindrical flows across various asymmetric notched structures through numerical simulation and particle image velocimetry. The focus was on investigating the influence of the number of asymmetric grooves on the drag characteristics, including the mean drag, spectral characteristics, time-averaged streamlines, separation point prediction, time-averaged pressure, wake vortex strength, Reynolds stress, and turbulent kinetic energy. The results showed that the presence of asymmetric grooves significantly influenced these flow parameters. Notably, the improvement was optimal in the four-groove configuration, evidenced by the lowest mean drag coefficient (0.804), vortex shedding frequency (2.74 Hz), recirculation area length (1.208D), and pressure difference across the cylinder (81.76). Moreover, this configuration resulted in the weakest trailing vortex, a 45% reduction in the maximum Reynolds stress (0.011), and a 40.5% decrease in the maximum turbulent kinetic energy (0.05). Thus, the presence of asymmetric grooves had a significant positive effect on the cylindrical flow properties, though the degree of improvement decreased with further increase in the number of grooves.

Article History

Received October 16, 2023

Revised January 21, 2024

Accepted February 1, 2024

Available online March 27, 2024

Keywords:

Asymmetrically grooved cylinder

Flow around a cylinder

Particle image velocimetry

Drag reduction

Recirculation region

1. INTRODUCTION

In marine engineering, the installation of offshore wind power infrastructure, submarine oil and gas pipelines, and offshore bridges requires a significant number of pile legs for supporting such structures. The flow of water through these pile legs produces a winding resistance, which can cause the structures to tilt, swing, or destabilize, ultimately compromising their safety and stability. Moreover, numerous eddies and turbulence regions are formed, exerting significant hydrodynamic loads on offshore structures. This increases their maintenance and repair expenses and potentially jeopardizes their safety.

Generally, to reduce the flow-induced winding resistance of pile leg structures installed in a marine environment, the drag reduction is examined by simplifying the actual flow as a cylindrical one. In recent years, researchers have extensively investigated the use of grooved cylindrical surfaces to reduce drag by suppressing eddy currents. This involves machining grooves of various shapes and sizes on cylindrical surfaces. This method has additional benefits of being low cost and easy to implement. Li et al. (2022) investigated a turbulent

boundary layer flow over a semicircular grooved surface in terms of the mechanism of friction drag reduction. Particle image velocimetry (PIV) and hot-wire anemometry (HWA) were applied to analyze the flow data. The difference in the surface friction coefficient varied significantly at three free-flow velocities for corrugation spacings of 17, 31.3, and 50.4 units. It decreased by 5.75%, increased by 0.3%, and increased by 10.7%, respectively. A near-wall flow structure analysis showed a surge in the flow coherence and a reduction in the spatial connections between turbulent formations near the wall in a drag-reduced state. The energy spectrum of the flow showed that coherent structures within an internal unit wavelength ranging from 100 to 300 close to the wall exhibited an increase in the energy content for the drag increase mechanism.

Wang et al. (2021) investigated the concept of “vortex-driven design” and a design approach for micron and nanoscale trench surface structures as well as a drag reduction method for bio-inspired trench surface structures. The author proposed a design strategy for micron and nanoscale groove surface patterns along with the “vortex-driven design” concept. Numerical simulations

Nomenclature		
k	turbulent kinetic energy	Y^+ dimensionless number of heights from the wall of the cylinder to the nearest mesh node
σ_k	turbulent Prandtl constant	Re Reynolds number
ω	turbulent kinetic energy dissipation rate	$\overline{C_d}$ average drag coefficient
μ	dynamic viscosity	St Strouhal number
β	model constant	η drag reduction rate
D	characteristic length of the cylinder	L_R length of recirculated area
Δy	height of the first layer of the grid	η drag reduction rate
$\overline{C_{d,smooth}}$	average drag coefficient of smooth cylinder	$\overline{C_{d,groo}}$ average drag coefficient of asymmetrically grooved cylinder
Δt	time step size	f frequency
ρ	density	

showed a significant decrease in the average frictional resistance of the nested groove surface structure, with the greatest decrease reaching 18.76%. As part of this study, a novel modification to a drag reduction material was also proposed. Priyadarsan and Afzal (2023) investigated the impact of groove modification on cylinders. They demonstrated three primary notch types, namely pits, squares, and triangles, at Reynolds numbers of 100, 150, and 200. The square notch produced higher drag and lift reductions, particularly at the 90° position. Although all notch locations exhibited a viscous drag reduction, those on the flow-ward side of the cylindrical surface showed increased pressure drag. The vorticity pattern presented more irregularities, and the separation angle was likewise impacted. In conclusion, to reduce the hydrodynamic drag and lift, a notch modification can serve as a passive control method.

Becheffar and Chaib (2023) investigated the impact of roughness on the hydrodynamics around a notched cylindrical surface to reduce wind loading. They numerically investigated the steady-state laminar flow over a cylinder with varying numbers of triangulation notches along its circumference, and the predicted outcomes were validated. Zheng et al. (2023) investigated the use of surface-patterned textiles to mitigate the noise and drag in a cylinder. Various experiments were conducted in an anechoic wind tunnel at Reynolds numbers between 2×10^4 and 1.6×10^5 . The noise and drag could be reduced simultaneously but at Reynolds numbers that corresponded to various cylindrical flow regimes. Moreover, the data collected from microphone arc arrays indicated that the primary factor contributing to noise reduction was the suppression of wind-forming sound. Subsequent investigations revealed substantial alterations to the flow dynamics, shedding light on the differences in both the drag and noise under varying flow regimes. A wide variety of surface-patterned textiles can be effective in reducing both the drag and noise in cylinders, with optimal outcomes achieved by considering the Reynolds number. Zhang et al. (2022a) studied the effect of helical fluted surfaces on wind drag reduction in cylindrical objects, specifically under typhoon conditions. The results of wind tunnel tests revealed a decrease in the wind

resistance coefficient of the cylinders, particularly at the critical Reynolds number, which ranges from approximately 9.3×10^4 to 1.1×10^5 . The presence of shallow grooves and a few spirals was found to effectively reduce the drag coefficient under typhoon conditions.

A large-eddy simulation can help approximate the flow separation and turbulence around a cylinder and determine its flow characteristics, pressure coefficient, surface friction coefficient, drag coefficient, and Q-standard field. Soylar et al. (2022) conducted a comparative study utilizing experimental and CFD numerical simulation techniques to examine the wake structure of a rectangular slotted cylinder and a smooth cylinder with roughness coefficient (ϵ/D) values of 0.02, 0.04, and 0.06. The experiments were conducted at a Reynolds number (Re) of 5000, whereas the numerical simulations were performed in the Re range of 5000–20000. Compared with the smooth cylinder, the rectangular slotted cylinder had its saddle point positioned nearer to the surface. Moreover, the highest roughness led to a 30% reduction in the time-averaged drag coefficient at $Re = 20000$. This study demonstrated the effectiveness of incorporating rectangular grooves in a cylindrical structure to reduce the time-averaged drag coefficient.

A bionic structure is a promising avenue for drag reduction research. Zhang et al. (2022b) developed bionic models G and GM, inspired by fish scales and mucous membranes, to reduce frictional drag. These models comprised a groove structure and a mucous membrane. A large-eddy simulation confirmed the effectiveness of the bionic structures in reducing the turbulent drag. At a Reynolds number of approximately 780, the GM structure exhibited a 2% higher drag reduction than the G structure. At a Reynolds number of approximately 1250, this value increased to 8%. The GM structure, with increasing effectiveness at higher Reynolds numbers, proved superior to the G structure. Another example is the air flow around bird wings during flight, which can be characterized by a winding flow. The air flow benefits from the non-smooth structure of the feathers, enhancing flight dynamics and stability while reducing resistance. Qi (2020) designed an asymmetrically grooved structure

inspired by bird feathers. However, the study focused only on the winding characteristics of smooth and asymmetrically grooved cylinders, neglecting the impact of the variations in the parameters related to the grooved structure on drag reduction in cylindrical windings. Moreover, experimental validation is lacking.

In this study, the aforementioned gaps in literature were addressed by reconstructing an asymmetrically grooved structure, varying the number of grooves on the cylinder, and analyzing its winding resistance reduction through numerical and experimental methods. By employing numerical simulation and PIV, the objective of this research was to assess the impact of the number of asymmetrical grooves on the drag reduction characteristics of cylindrical windings. The drag reduction characteristics of cylindrical flows around surfaces featuring different numbers of asymmetrical grooves were explored. The focus was on investigating parameters such as the mean drag coefficient, spectral characteristics, time-averaged streamlines, separation point prediction, time-averaged pressure, wake vortex strength, Reynolds stress, and turbulent kinetic energy (TKE). The results provide insights into the design of pile legs installed in marine environments.

2. NUMERICAL SIMULATION METHODOLOGY

2.1 Turbulence Modeling

In this study, the $k-\omega$ shear stress transport (SST) model (Menter et al., 2003) was used for the numerical simulations. The corresponding model equation can be expressed as follows:

$$\frac{D\rho k}{Dt} = \tau_{ij} \frac{\partial u_i}{\partial x_j} - \beta^* \rho k \omega + \frac{\partial}{\partial x_j} \left[(\mu + \sigma_k \mu_t) \frac{\partial k}{\partial x_j} \right] \quad (1)$$

$$\frac{D\rho \omega}{Dt} = \frac{\gamma}{v_t} \tau_{ij} \frac{\partial u_i}{\partial x_j} - \beta \rho \omega^2 + \frac{\partial}{\partial x_i} \left[(\mu + \sigma_\omega \mu_t) \frac{\partial \omega}{\partial x_j} \right] + 2(1 - F_1) \rho \sigma_{\omega 2} \frac{1}{\omega} \frac{\partial k}{\partial x_j} \frac{\partial \omega}{\partial x_j} \quad (2)$$

Here, ρ is the fluid density; k is the TKE; μ and μ_t

denote the dynamic viscosity and turbulent viscosity of the fluid; σ_k and σ_ω denote the turbulent Prandtl constants; ω is the dissipation rate; β is a model constant.

2.2 Geometric Model and Boundary Conditions

In the study, the angle of the asymmetrically grooved structure was modeled after a dune structure (Parsons et al., 2004). As shown in Fig. 1, the angle between the OQ and QM is 55° , and the angle between the OQ and QN is 70° .

Figure 2 shows a cross-sectional diagram of cylinders with different numbers of asymmetric grooves, including a smooth cylinder (Case 1) and three grooved cylinders (Cases 2, 3, and 4) with a groove depth of $0.015D$. Case 2 comprises four grooves, whereas Cases 3 and 4 have twelve and twenty-four grooves, respectively.

The rectangular computational domain considered in this study covers an area of $20D$ in the current direction and $10D$ transversely. The center of the cylinder is located $15D$ away from the flow field outlet, with the wall located $5D$ away from each side of the cylinder. The distance between the inlet of the flow field and the center of the cylinder is $5D$. The cylinder diameter (D) is 20 mm. The computational domain input is a velocity input, while the

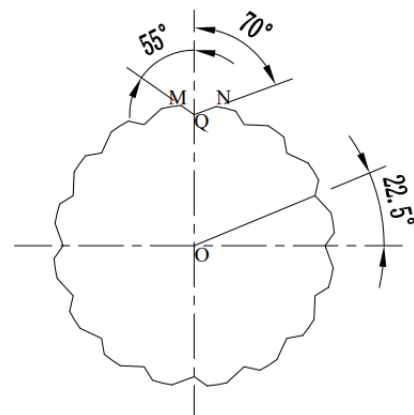


Fig. 1 Asymmetric groove structure angle design schematic

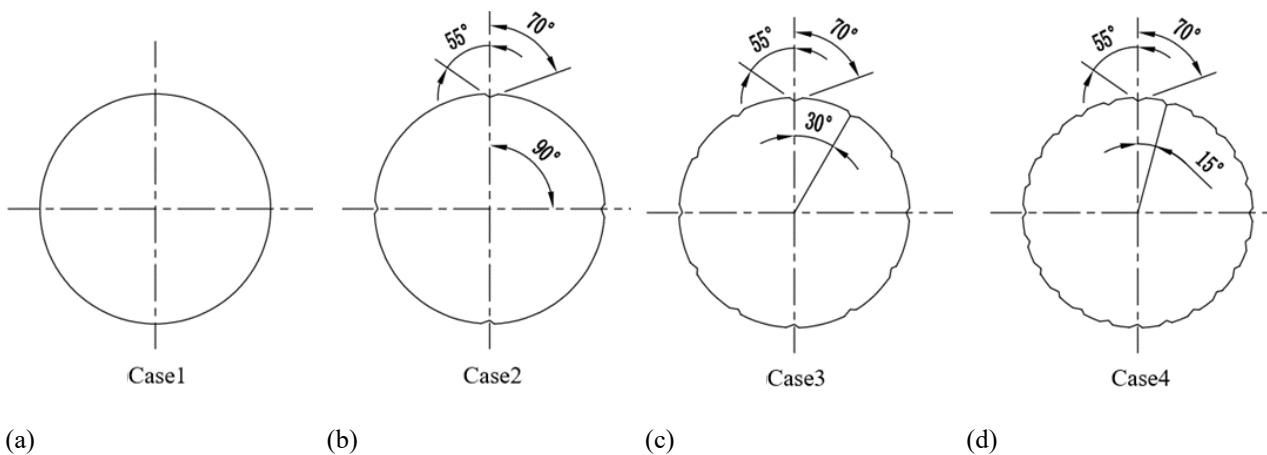


Fig. 2 Schematic diagram of the cylinder cross-section. (a) Case1: smooth cylinder, (b) Case2: asymmetrically grooved cylinder with 4 grooves, (c) Case3: asymmetrically grooved cylinder with 12 grooves, (d) Case4: asymmetrically grooved cylinder with 24 grooves

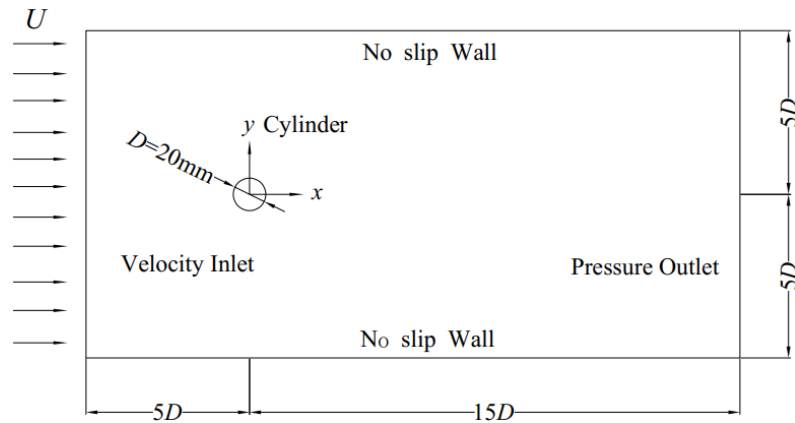


Fig. 3 Schematic diagram of computational domain

Table 1 Grid independence verification for the smooth cylinder at $Re=6 \times 10^3$

The first layer height	Mesh expansion ratio	Number of cells	$\overline{C_d}$		St	
			value	Deviation/%	value	Deviation/%
0.054mm densify 40 layers mesh for the location with asymmetric groove	1.3	90875	1.189	+21.2	0.25	+18.4
	1.2	122945	1.016	+3.56	0.221	+4.7
	1.1	168520	0.981	-	0.211	-
	1.05	179245	0.979	-0.2	0.21	-0.4

computational domain outlet is designated as the pressure outlet. The cylinder is treated as a fixed boundary, with non-slip walls present at both the front and rear. Figure 3 shows the details of the boundary conditions of the computational domain.

Before meshing, it is necessary to estimate the height of the first grid layer on the cylindrical wall surface while ensuring that the grid quality satisfies the given requirements to minimize the inaccuracies in the numerical simulation. In the SST $k-\epsilon$ turbulence model, a Y^+ value of approximately 1 for the distance between the cylindrical wall surface and the closest grid node is frequently required (Zou, 2008). Y^+ with respect to the height of the first grid level can be represented by:

$$Y^+ = 0.172 \frac{\Delta y}{D} Re^{0.9} \tag{3}$$

The height of the first-level grid measured 0.054 mm, which was calculated according to the formula. To minimize errors, a grid-independence test was conducted following the meshing process. The number of meshes was determined based on the extension ratio and the number of nodes employed.

An analysis of the data, listed in Table 1, showed that reducing the ductility ratio from 1.1 to 1.05 had little effect on the average drag coefficient, which only increased by 0.2%. However, the mesh increased significantly by approximately 6%. Notably, in this instance, increasing the number of meshes did not significantly affect the calculation accuracy but only contributed to an increase in the computational volume of the numerical simulation. When increasing the ductility from 1.1 to 1.2 and 1.3, the mesh reduced by 27% and 46.07%, respectively.

Concurrently, the average drag coefficient increased by 3.56% and 21.2%. This demonstrates that an excessive focus on attaining a smaller mesh number would result in the computational accuracy. Therefore, the extension ratio was determined to be 1.1 in this study, and subsequently arrived at a mesh count of 168,520. Figure 4 shows the mesh distribution and localized expansion of the smooth and asymmetrically grooved cylinders.

To ensure the accuracy of the numerical simulation findings, the numerical simulation results of the smooth cylinder at $Re = 6 \times 10^3$ were compared with the experimental results obtained by Schewe (1983) and Zdravkovich (1981). The average drag coefficient and Strouhal number (St) were analyzed. The average drag coefficient deviated from the experimental result Zdravkovich (1981) of $\overline{C_d} = 0.9$ by only 9% and from the experimental result Schewe (1983) of $St = 0.2$ by only 5.5%. This shows that the numerical simulation results are in good agreement with the experimental results, confirming the reliability and accuracy of the simulation technique used in the study.

The calculation was set up using the Fluent Solver as follows. The simulation was performed in two dimensions. The fluid medium was water with a density (ρ) of 998.2 kg/m^3 , the dynamic viscosity (μ) was $1.01 \times 10^{-3} Pa \cdot s$, and the inlet flow rate was 0.3 m/s. The pressure-velocity-coupled SIMPLE discrete method was employed. The solution format was a windward format discretized to the second-order with a convergence standard of 1×10^{-6} . The steady-state calculation was first performed. After approximately 150 cycles of vortex shedding following the cylinder, the flow field in the steady state became

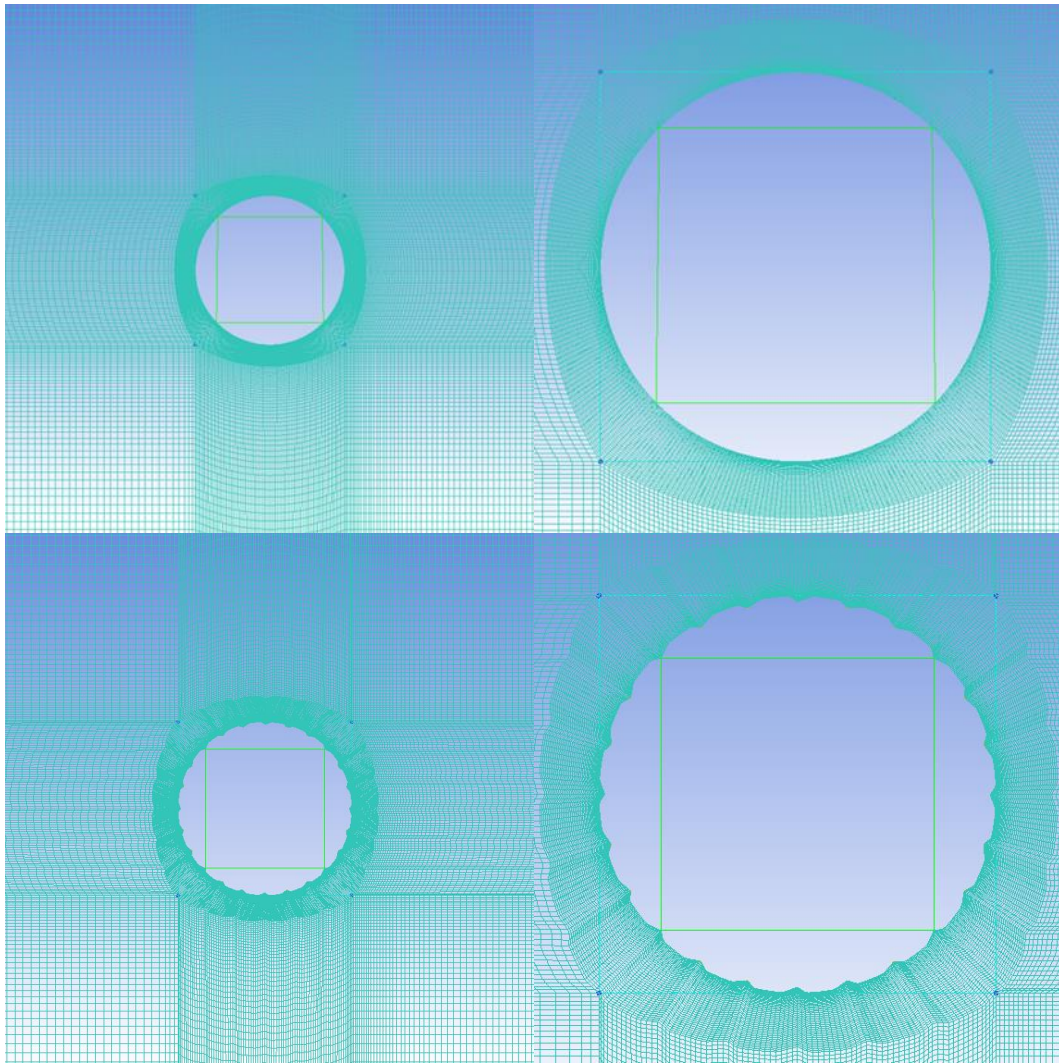


Fig. 4 The diagram of the mesh division and the partial enlargement of the mesh

Table 2 Drag reduction of asymmetric groove cylinders with different numbers of grooves

Number of asymmetric grooves	$\overline{C_d}$	η
0	0.981	—
4	0.804	+18.04%
12	0.886	+9.68%
24	0.949	+3.26%

stable. Subsequently, transient calculations were made based on this stable state to minimize the computational error and ensure more accurate results. The time step was set using the following equation:

$$\Delta t = \frac{1}{20f} \quad (4)$$

3. NUMERICAL SIMULATION FINDINGS AND DISCUSSIONS

3.1 Average Resistance Coefficient

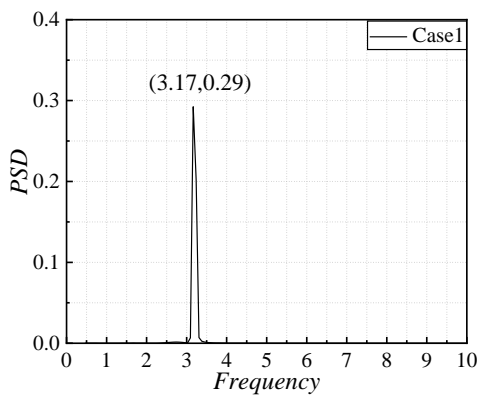
Table 2 shows a comparison of the drag reduction effects for cylinders with different numbers of asymmetric grooves. The comparative analysis shows that the drag

coefficients of the smooth and asymmetrically grooved cylinders are 0.981, 0.804, 0.886, and 0.949. The drag coefficients gradually increased with an increase in the number of grooves, leading to a lower rate of drag reduction. When four asymmetric grooves are present, the average drag coefficient is minimized to 0.804. At this point, the drag reduction rate (η) is +18.04%, representing the optimum drag reduction effect.

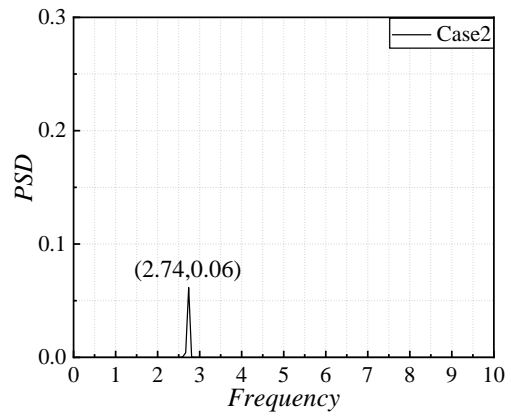
$$\eta = \frac{\overline{C_{d_{smooth}}} - \overline{C_{d_{grooved}}}}{\overline{C_{d_{smooth}}}} \times 100\% \quad (5)$$

3.2 Analysis of Spectral Characteristics

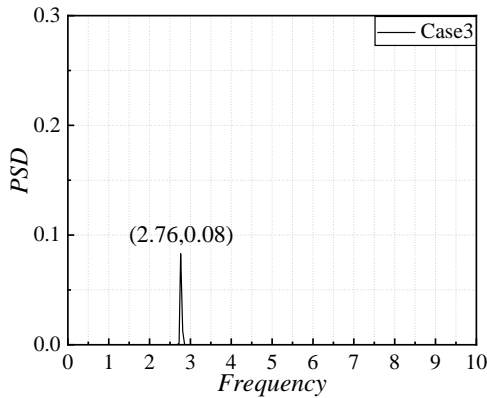
The power spectral density (PSD) was extracted by analyzing the lift coefficient using the fast Fourier transform (FFT) method, from which the frequencies of



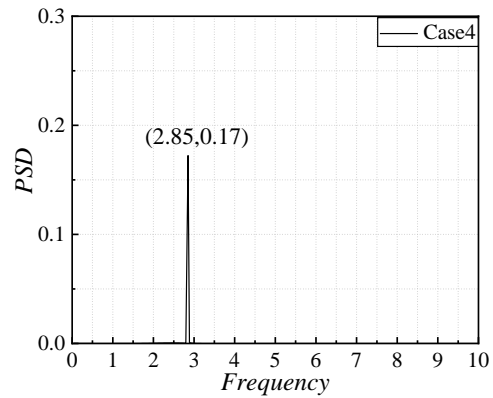
(a) Smooth cylinder



(b) Asymmetrically grooved cylinder with 4 grooves



(c) Asymmetrically grooved cylinder with 12 groove



(d) Asymmetrically grooved cylinder with 24 grooves

Fig. 5 Power spectrum density of lift coefficients for a smooth cylinder and asymmetrically grooved cylinders with different numbers of grooves

wake vortex shedding were obtained for the smooth cylinder and for cylinders with different numbers of asymmetric grooves. Figure 5 shows the PSDs for the lift coefficients of these cylinders. A comparative analysis of the results shows that cylinders with different numbers of asymmetric grooves exhibited lower dominant frequencies of vortex shedding than the smooth cylinder. The recorded values are 3.17, 2.74, 2.76, and 2.85 Hz, which correspond to dimensionless numbers (*St*) of 0.211, 0.182, 0.184, and 0.19, respectively; their corresponding peak PSDs are also lower than that of the smooth cylinder, with values of 0.06, 0.08, and 0.17, respectively, while the peak PSD of the smooth cylinder is 0.29.

A comparative analysis of the results shown in Fig. 6 reveals that the dominant frequencies of cylindrical vortex shedding for cylinders with different numbers of asymmetric grooves are reduced by 13.56%, 12.93%, and 10.09%, respectively. The PSDs of the main frequencies of cylindrical vortex shedding exhibit reductions of 79.31%, 72.41%, and 41.38% for cylinders with different numbers of asymmetric grooves, respectively. These results indicate that the suppression effect of the asymmetric grooves on the frequency of cylindrical vortex shedding gradually decreases with increasing number of grooves.

The findings suggest that the incorporation of asymmetric grooves in a cylindrical structure decreases

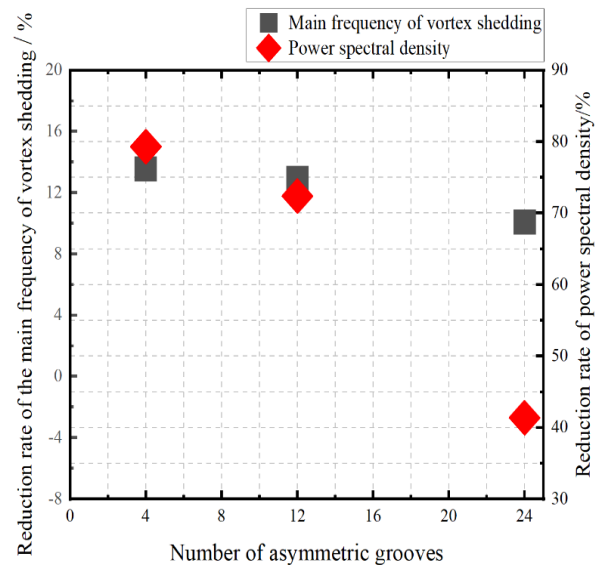


Fig. 6 Frequency of vortex shedding and corresponding power spectral density reduction rate for different numbers of grooves

the dominant vortex shedding frequency and thereby improves the suppression of vortex-induced vibration, with the suppression effect being optimum when the structure has four asymmetric grooves.

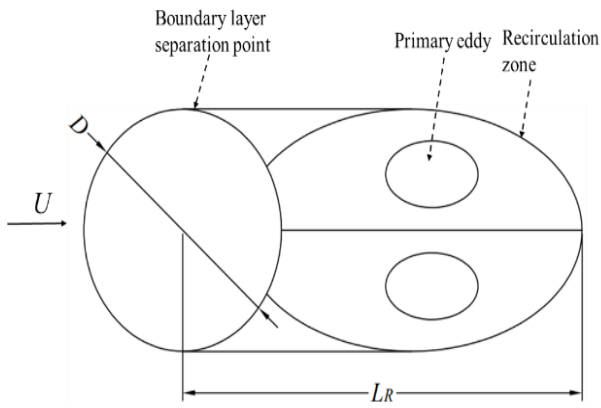


Fig. 7 Schematic diagram of the recirculation region

3.3 Time-Averaged Streamlines Analysis

Figure 7 illustrates the schematic of the time-averaged flow structure of a cylindrical bypass flow. L_R indicates the length of the recirculated area, defined as the length between the center of the cylinder and the seat position (Tonui & Sumner, 2009).

To understand the impact of asymmetrical groove structures on the wake area, this section presents a comparative analysis of the time-averaged flowlines. Figure 8 shows the time-averaged flow lines for smooth cylinders and different quantities of asymmetrical grooved cylinders. A comparative analysis shows that cylinders with different numbers of asymmetric grooves have recirculation zone lengths of $1.208D$, $1.336D$, and $1.72D$, respectively. These lengths are comparably shorter than that of smooth cylinders, which measures $1.948D$.

The asymmetrically grooved structure can cause a displacement in the location of the interfacial separation point, resulting in a reduction in the recirculation area. Compared with cylinders having different numbers of asymmetric grooves, the cylinder with four grooves exhibited the shortest recirculation zone length. The length reduced by 37.98% in comparison with a smooth cylinder. This is due to the greater interference of small vortices in the asymmetric grooves with the formation of large vortices at this number.

3.4 Separation Point Prediction

The boundary layer fluid will separate from the wall flow if the fluid viscous force in the cylindrical wall boundary layer is lower than the inertial force of the fluid and form an unstable shear layer. This will lead to the formation of a wake zone in the backward direction. The size of the wake zone has a direct impact on the differential pressure drag, making it a crucial factor (Zhou et al., 2015). The size of the wake zone decreases as the separation location moves further downstream, resulting in a lower differential pressure drag. To modify the distribution pattern of fluid motion within the bounding layer, several asymmetrically grooved structures are positioned on the cylindrical surface. This arrangement effectively regulates the fluid motion.

Figure 9 shows the diagram used for monitoring the separation point. The monitoring angle is measured in relation to the flow direction, and the initial monitoring position is fixed at $\theta = 0^\circ$. The angle range spans between 0° and 180° . Figure 10 shows the predicted angle of the fluid separation point on a smooth cylindrical surface, featuring a separation point angle of 86.48° .

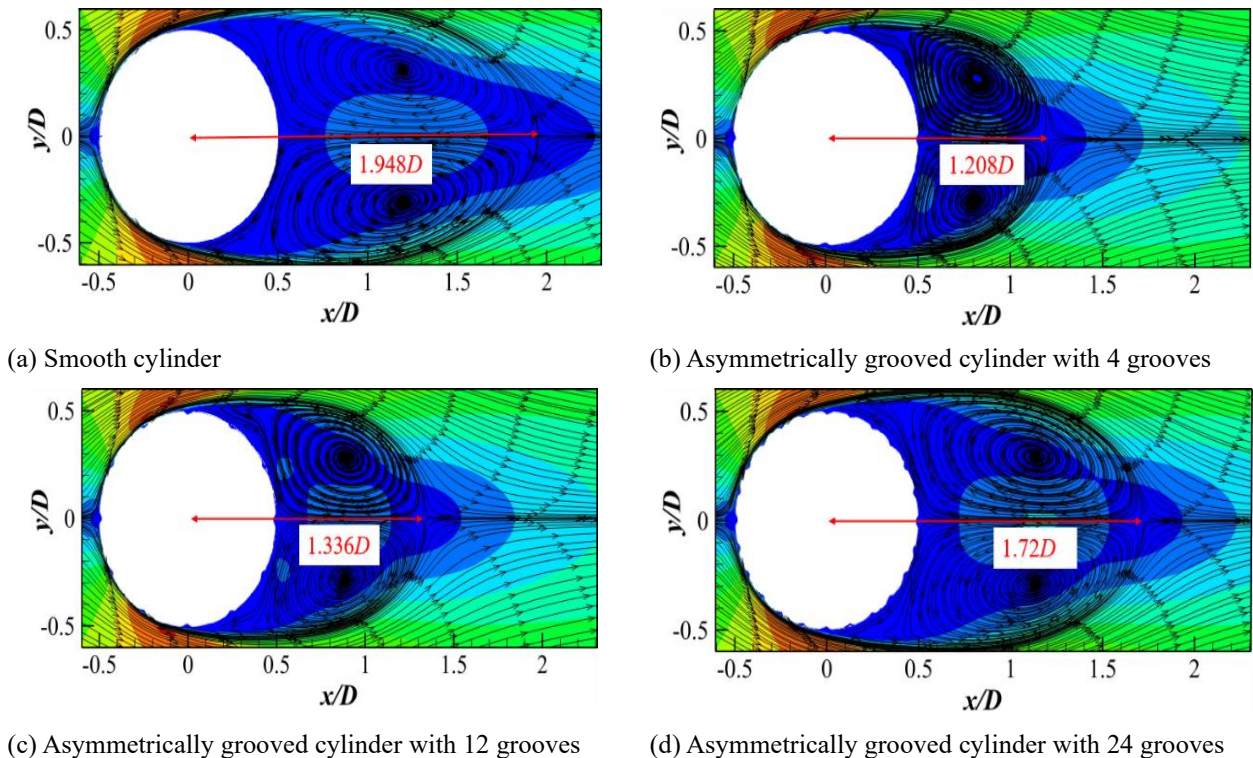


Fig. 8 Time-averaged streamline for a smooth cylinder and asymmetrically grooved cylinders with different numbers of grooves

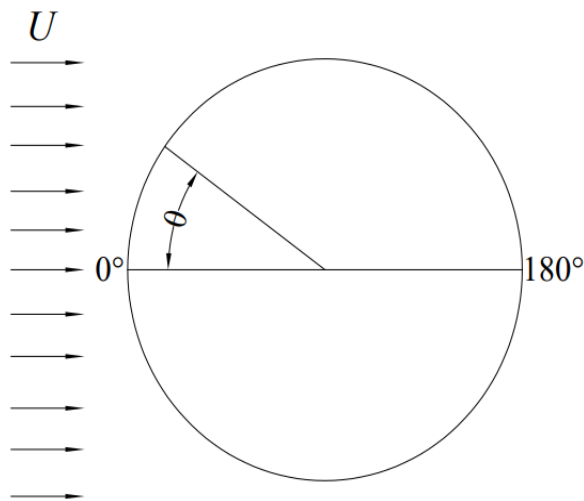


Fig. 9 Diagram of separation point

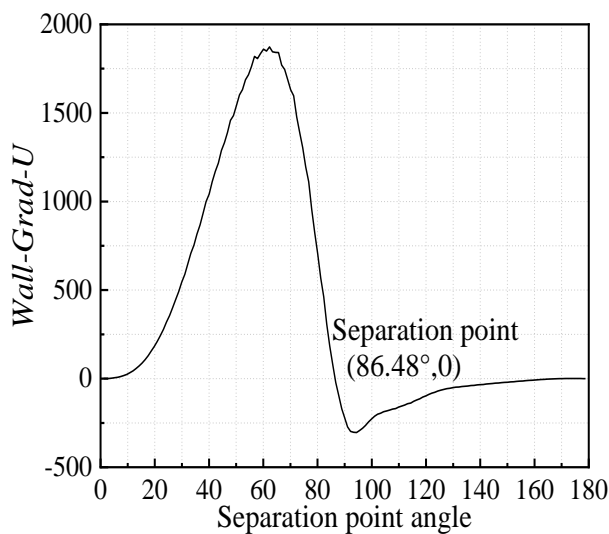


Fig. 10 Predicted separation point of the surface of a smooth cylinder

Figure 11 shows a comparison of the separation points for smooth and asymmetrically grooved cylinders with different numbers of grooves. Clearly, with an increase in the number of grooves, the angle of separation between the asymmetrically grooved cylinders and the smooth cylinder gradually increases. Among the asymmetric groove cylinders, the one with four grooves exhibited the lowest drag coefficient and the closest separation point to the downstream. This suggests that the point at which the asymmetrically grooved cylinder end is closer to the downstream section the smooth cylinder, due to its lower drag coefficient.

3.5 Time-Averaged Pressure Analysis

When fluid flows on the surface of a cylinder, a pressure differential is developed in front of and behind it. The more modest the pressure differential between the front and back of the cylinder, the lower the drag in the bypass flow. Figure 12 shows the time-averaged pressure distribution on a smooth cylinder and on cylinders with different numbers of asymmetric grooves. A comparative

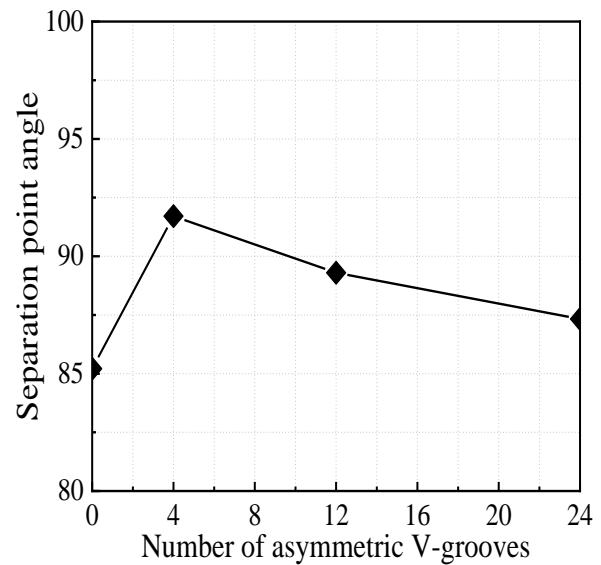


Fig. 11 Comparison of separation points for a smooth cylinder and asymmetrically grooved cylinders

analysis of the results reveals the front-to-back pressure differences for cylinders with different numbers of asymmetric grooves: 81.76, 83.67, and 85.46. In comparison, the front-to-back pressure difference for the smooth surface cylinder was 92.46. The pressure difference between the front and back of the cylinders with asymmetrical grooves was lower than that in the case of the smooth cylinder. This confirms that the asymmetrical groove structure helps reduce the pressure difference between the front and back, thereby achieving drag reduction. The cylinder with four asymmetrical grooves exhibited the least pressure difference between the front and rear, resulting in a reduction of 11.57% compared with the smooth cylinder. This suggests that it has the most effective impact on drag reduction.

3.6 Trailing Vortex Intensity Analysis

In a cylindrical winding wake, two high-vorticity regions with numerically opposite values are distributed along the flow direction. These regions can be considered as vortex structure distribution areas (Yu, 2010). Since vortex quantities have positive and negative values, it is necessary to introduce a vortex intensity field that depicts only the intensity of the vortex without any positive or negative difference. Figure 13 shows the vortex intensity distribution of the trailing vortex for a smooth cylinder and for cylinders with different numbers of asymmetric grooves at a specific moment. The smooth cylindrical wake exhibits two considerable vortices, which correspond to the mushroom rib structure reported by Wang and Zhou (2009). When examining cylindrical trails, it is apparent that the peak intensity of the trailing vortex is lower for asymmetric groove cylinders in comparison with smooth cylinders. Moreover, the two peak positions are relatively widespread. Among the cylinders with different numbers of asymmetric grooves, the cylinder with four grooves has the lowest peak intensity of the trailing vortex.

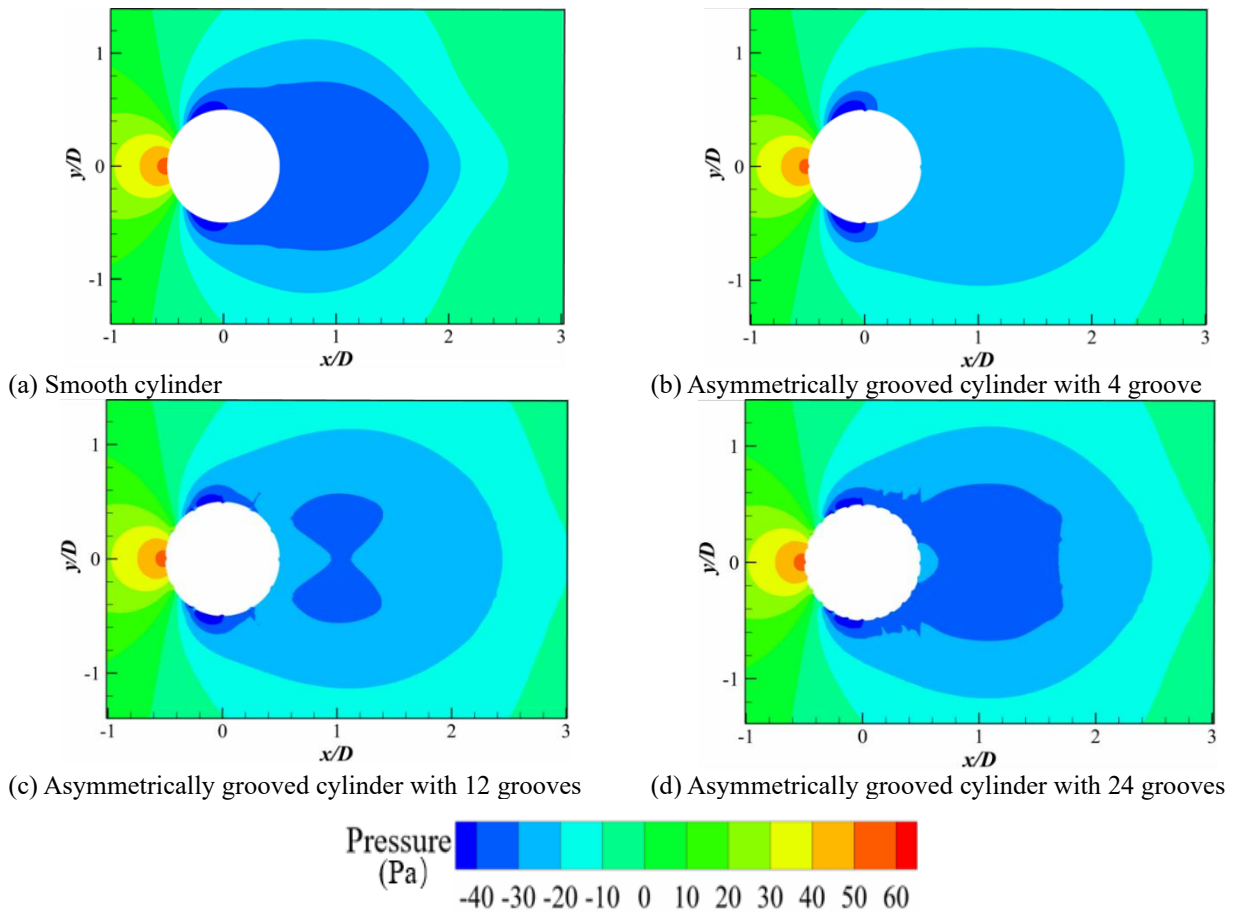


Fig. 12 Time-averaged pressure diagram of a smooth cylinder and asymmetrically grooved cylinders with different numbers of grooves

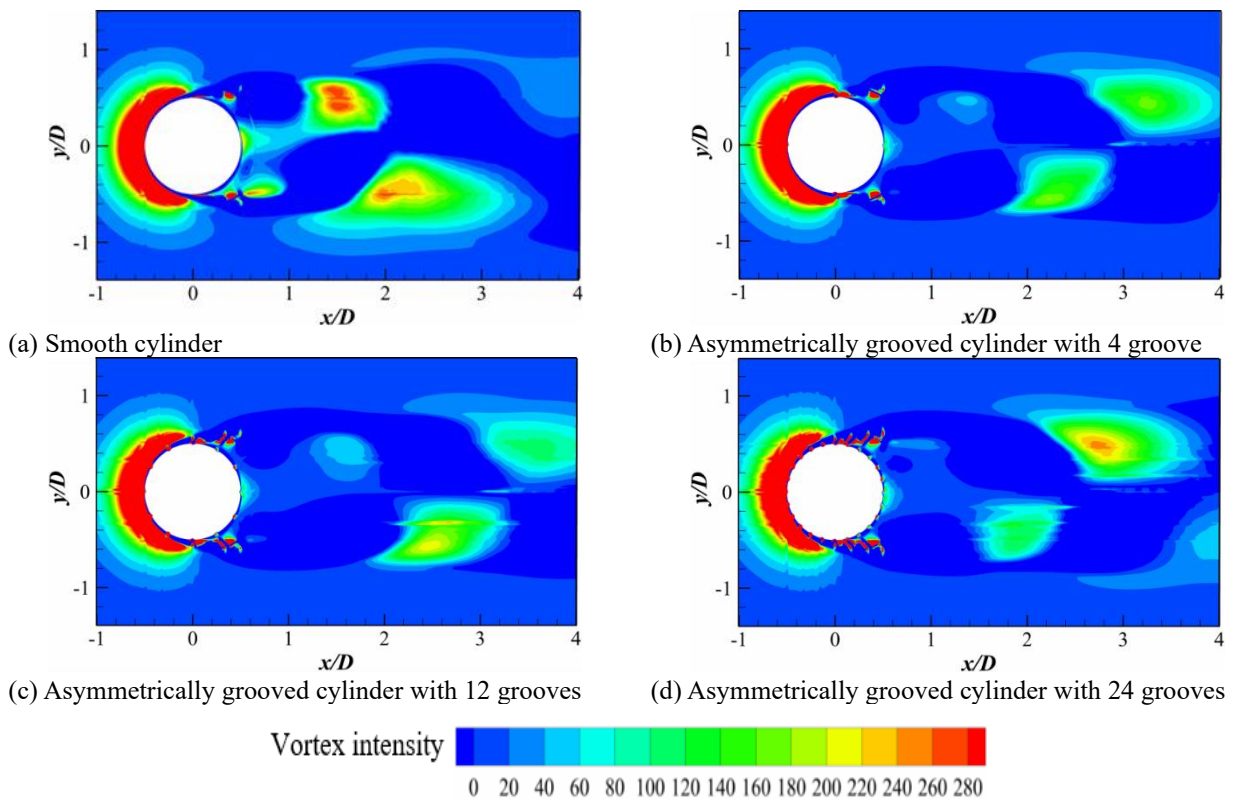
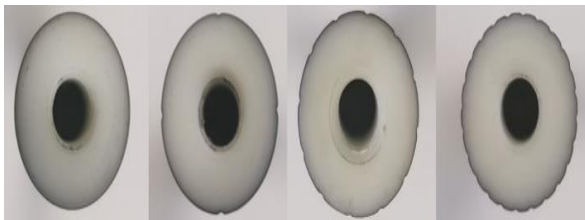


Fig. 13 Trailing vortex intensity distribution of a smooth cylinder and asymmetrically grooved cylinders with different numbers of grooves



(a) Top view of workpiece



(b) Cross section of workpiece

Fig. 14 Display of the finished cylinder workpiece

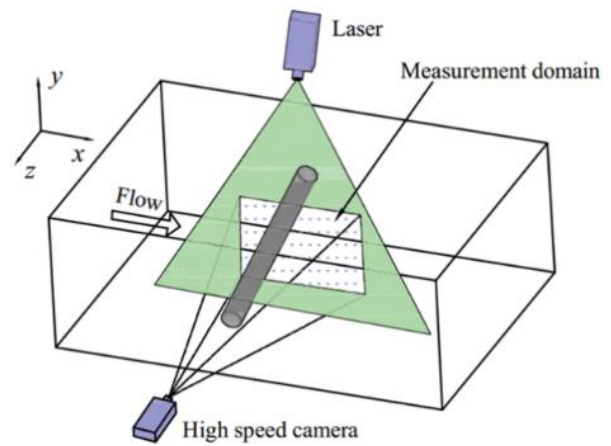
4. POST-EXPERIMENTAL PROCESSING FINDINGS AND DISCUSSION

4.1 Experimental Apparatus

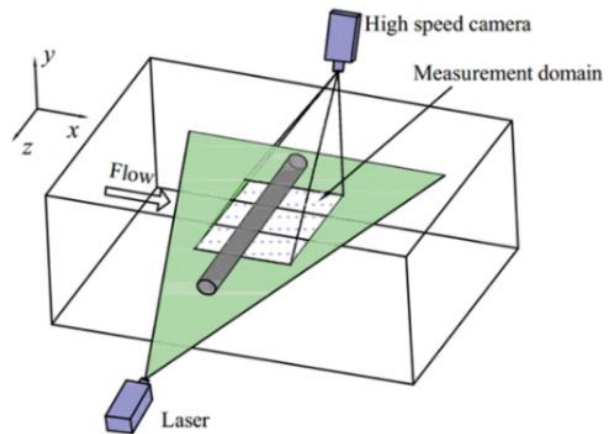
In this study, the PIV was employed to perform experiments on smooth cylinders with a Reynolds number of 6×10^3 as well as on cylinders with different numbers of asymmetric grooves to compare their respective wake structures. The diameter (D) of the cylindrical model in the experiment was 20 mm, the length (L) was 300 mm, and its material was polyvinyl chloride (PVC). Figure 14 shows the physical illustration of the workpiece.

The PIV measuring technology was utilized to capture the flow-domain information in the (x, y) and (x, z) planes of the cylindrical wake. Figure 15 shows the schematic layout of the PIV measurement plane. The flow, lateral, and longitudinal directions are represented using the x , y , and z coordinates, respectively. The data were collected in the flow direction level (x, y) and the propagation level (x, z) , as shown in Figs. 15(a) and (b), respectively.

The PIV technology helped visualize the cylindrical wake via a recirculating fluid tank situated within the PIV facility. Figure 16 shows a schematic of the PIV recirculating water tank experiment. The experimental section is a rectangular cross-section, measuring 0.3 m \times 0.4 m (width \times height). The flow rate and volume flow were adjustable via the included control cabinet. To allow the laser beam produced by the laser instrument to pass through, the walls and bottom of both the sides of the tank were constructed from 10 mm-thick glass. Figure 17 shows the experimental site.



(a) (x, y) Planar flow field measurement layout



(b) (x, z) Planar flow field measurement layout

Fig. 15 Schematic diagram of PIV measurement plane

4.2 Time-Averaged Streamlines

Figure 18 shows a comparison between the time-averaged flow lines in the plane (x, z) at $y/D = 0$ for the smooth cylinder and various asymmetrically grooved cylinders. The reflux zone length that forms at $x/D = 1.654$, when the flow speed toward the end of the smooth cylinder was practically zero, was measured from the cylinder surface. Possibly due to the reconnection of the vortex splitting, which resulted in wave shedding, the region shown in the figure also exhibited a wave-like shape (Cao & Tamura, 2015).

For $x/D < 1.654$, the flow rate reverts to that of the fluid external to the wake, indicating compression of the negative flow range. The locations of the return zone dividers fluctuate depending on the number of asymmetric groove cylinders, and they are positioned at roughly $x/D = 1.15, 1.32, \text{ and } 1.52$. Table 3 shows a comparison of the reflux zone length for the asymmetrically grooved cylinders with different numbers of grooves. The formation length of the return zone for cylinders with the asymmetric grooves was shorter compared with that of the smooth cylinder. Among the cylinders with different numbers of asymmetric grooves, the one with four grooves had the shortest recirculation zone length, which was reduced by 30.47% compared with the smooth cylinder.

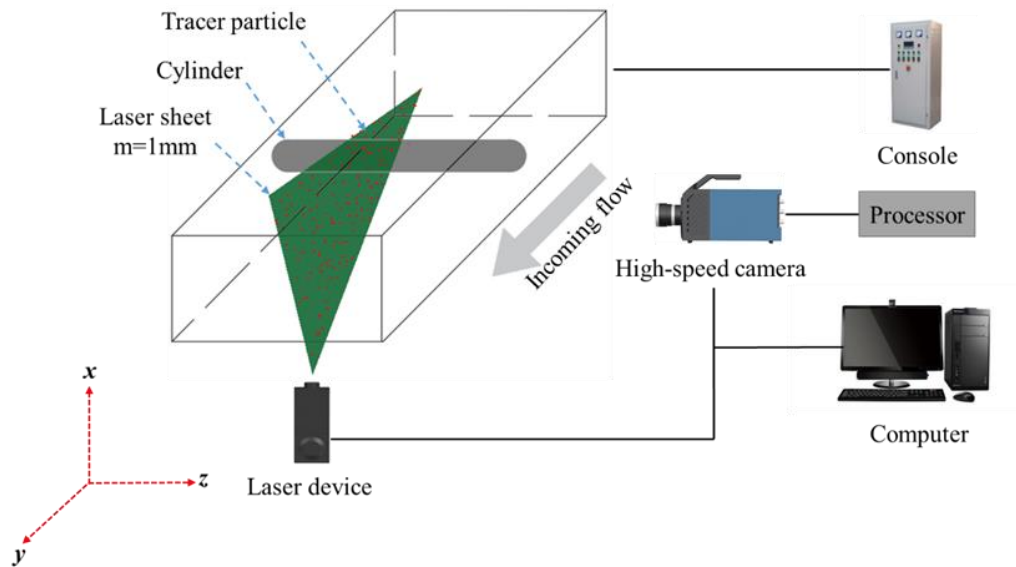


Fig. 16 PIV particle circulation water tank experiment

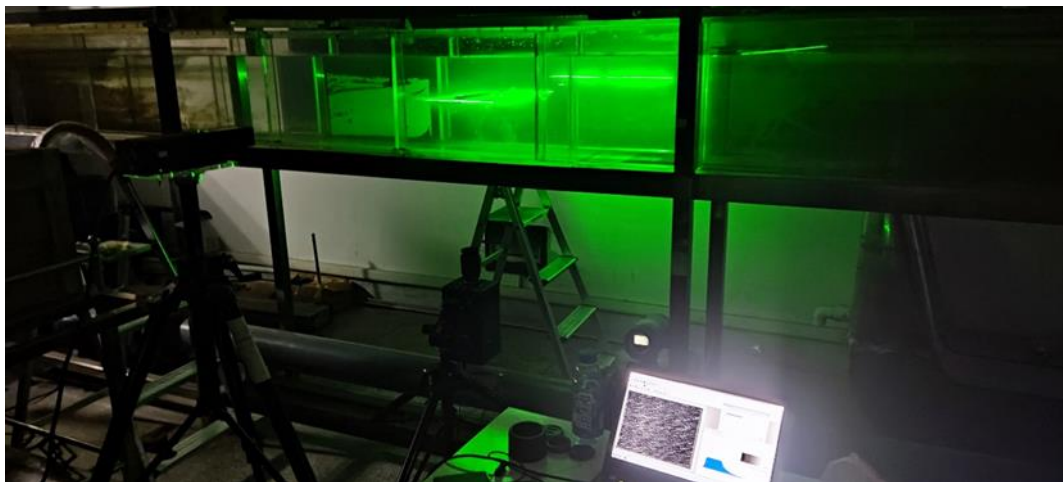


Fig. 17 Experimental site device diagram

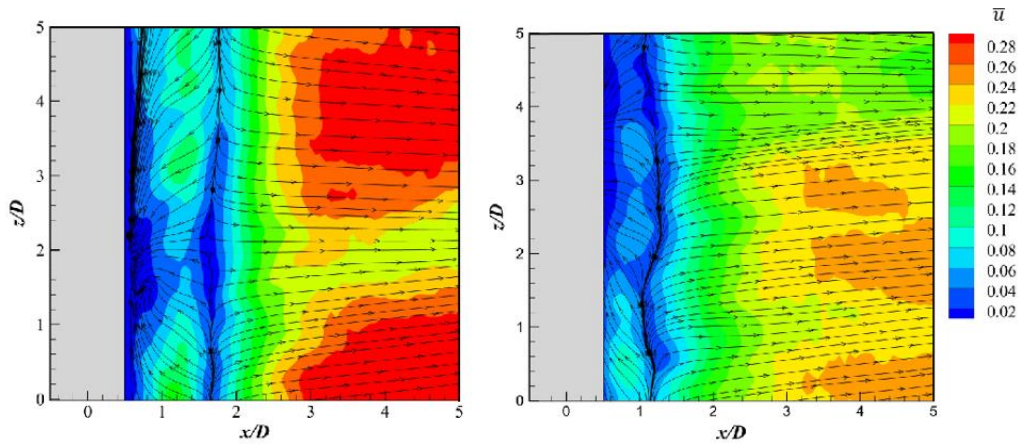
Table 3 Reflux zone length of asymmetric groove cylinders with different numbers of grooves

Number of asymmetric grooves	x/D	Deviation/%
0	1.654	—
4	1.15	-30.47
12	1.32	-20.19
24	1.52	-8.10

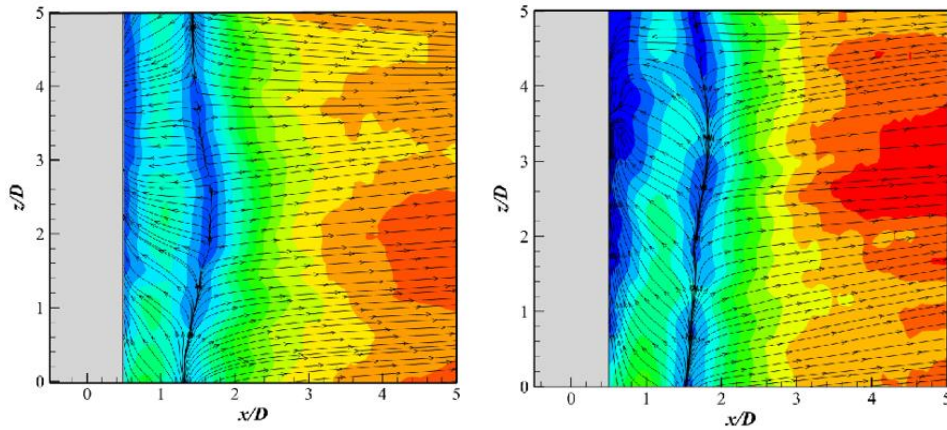
4.3 Spectral Characteristics

The PIV data were used to compute the spectra at the pulsation velocity point v for a more in-depth investigation of the flow structure. Figure 19 shows the spectra SV at positions $x/D = -1.7$, $y/D = 0.3$ of the speed component v in the tail of the smooth cylinder, and various numbers of asymmetrically grooved cylinders. The measurements were taken close to the path of flow toward the eddy. The pulsation velocities at their peaks for the smooth and asymmetrically grooved cylinders are as follows: 0.238, 0.12, 0.136, and 0.152. The corresponding frequencies are 3.003, 2.57, 2.61, and 2.71 Hz, which correspond to St values of 0.2, 0.171, 0.174, and 0.178, respectively. Table 4 shows a comparison of the spectral characteristics of the

asymmetrically grooved cylinders with different numbers of grooves. Clearly, there is a reduction in the flow pulsation velocity and frequency at the end of the cylinder. A significant reduction of 49.57% in the pulsation velocity and 14.41% in the vortex shedding frequency could be observed in the cylinder with four grooves. With asymmetrically grooved cylinders, two peaks become noticeable, and the main frequency of vortex shedding corresponds to a lower PSD compared with that in the case of the smooth column. The grooved structure is the cause of the phenomenon observed. Instability in velocity fluctuations is due to the notched structure, which limits the vortex formation length in the wake area. Consequently, there is a double-peak phenomenon.

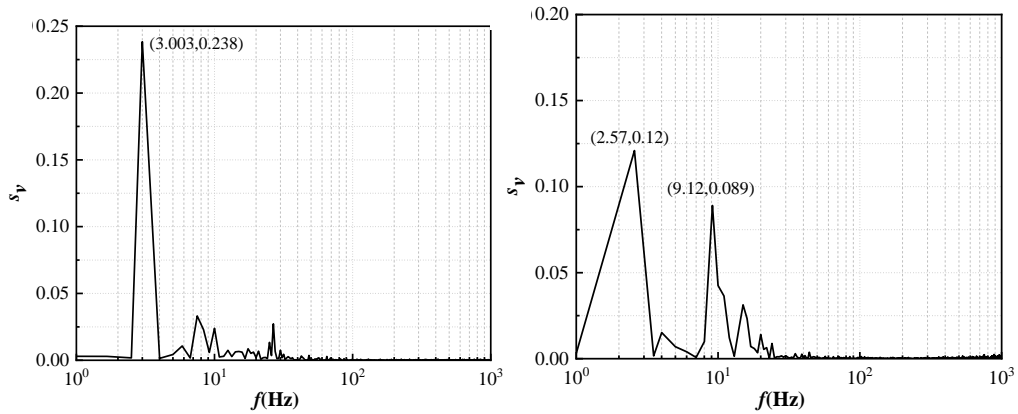


(a) Smooth cylinder (b) Asymmetrically grooved cylinder with 4 grooves

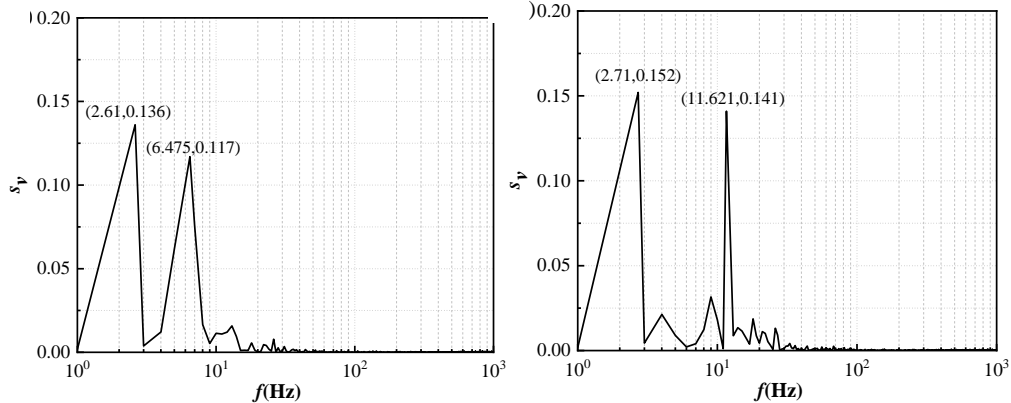


(c) Asymmetrically grooved cylinder with 12 grooves (d) Asymmetrically grooved cylinder with 24 grooves

Fig. 18 Time-averaged streamlines distribution in the (x, z) -plane



(a) Smooth cylinder (b) Asymmetrically grooved cylinder with 4 grooves



(c) Asymmetrically grooved cylinder with 12 grooves (d) Asymmetrically grooved cylinder with 24 grooves

Fig. 19 Spectral SV of velocity component v at $x/D = -1.7$, $y/D = 0.3$ and $z = 0$

Table 4 Spectral characteristics of asymmetric groove cylinders with different numbers of grooves

Number of asymmetric grooves	frequency		Peak pulsation velocity	
	value	Deviation/%	value	Deviation/%
0	3.003	—	0.238	—
4	2.57	-14.41	0.12	-49.57
12	2.61	-13.08	0.136	-42.85
24	2.71	-9.75	0.152	-36.13

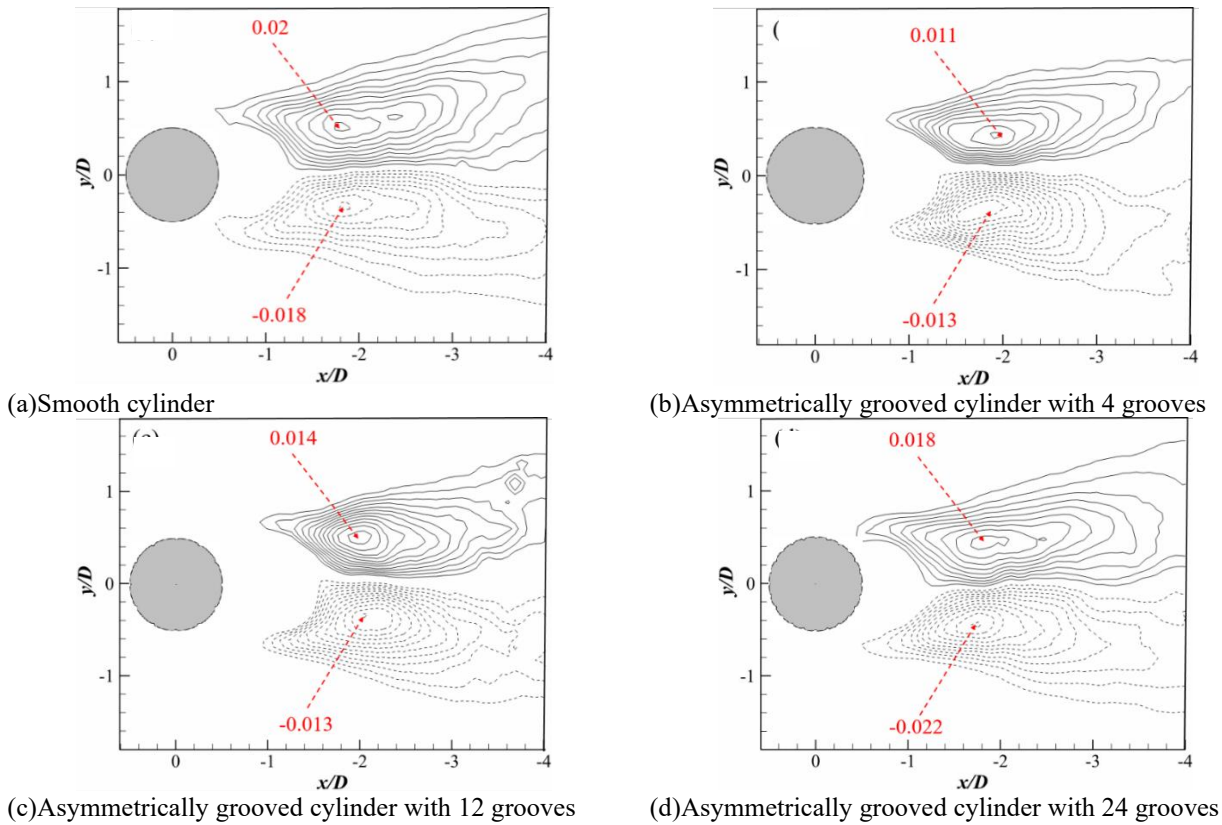


Fig. 20 Contours of the normalized Reynolds stress $\overline{u'v'}/U^2$ in the (x, y) -plane at $z/D=0$

4.4 Reynolds Stress

An essential aspect of the flow domain change representation is the Reynolds stress (Chen et al., 2023). Therefore, Reynolds stress contour plots were generated to explore the flow-domain properties on the smooth cylinder and asymmetric notched cylinders.

The Reynolds stress was obtained by decomposing the physical quantities within the turbulent flow into their mean value component over time and their fluctuating value component. An analysis of the Reynolds stress allows the stress profile associated with the flow domain to be investigated. Figure 20 shows the standardized distribution of the Reynolds stress of a smooth cylinder in the plane (x, y) and asymmetrically grooved cylinders with varying numbers. The Reynolds stresses of both the smooth and grooved cylinders are distributed symmetrically in the tail region near the centerline of the cylinder. As shown in Fig. 20, the smooth cylinder exhibits a maximum Reynolds stress of 0.002 and a minimum value of -0.011 . In contrast, the maximum Reynolds stress values of the various asymmetrically notched cylinders are reduced by 45%, 30%, and 10%, to approximately 0.011, 0.014 and 0.018, respectively.

This implies that the maximum Reynolds stress values are reduced for cylinders with different numbers of asymmetric grooves in comparison with the smooth cylinder. This is caused by the asymmetrically grooved structure influencing or changing the flow structure in the cylinder wake, reducing the turbulent fluctuations within the boundary layer (Rinoshika & Rinoshika, 2019). The highest drop in the maximum Reynolds stress value was observed in the cylinder with four asymmetric grooves. This suggests that the asymmetric notch structure at this number results in a greater reduction in turbulence fluctuations in the boundary layer. Therefore, the recirculation zone is controlled in cylinders with different numbers of asymmetric grooves, as shown in Fig. 8.

Figure 21 shows the dispersion of the Reynolds stress in the plane (x, z) comprising a smooth cylinder and asymmetric groove cylinders with various numbers of grooves. As shown in Fig. 21, the smooth cylinder exhibits a maximum Reynolds stress value of 0.0023 and a minimum value of -0.0019 . In comparison, cylinders with different numbers of asymmetric grooves generate maximum Reynolds stresses of 0.0013, 0.0015, and 0.002. Similarly, the corresponding cylinders have minimum Reynolds stress values of -0.0025 , -0.0025 , and -0.0021 ,

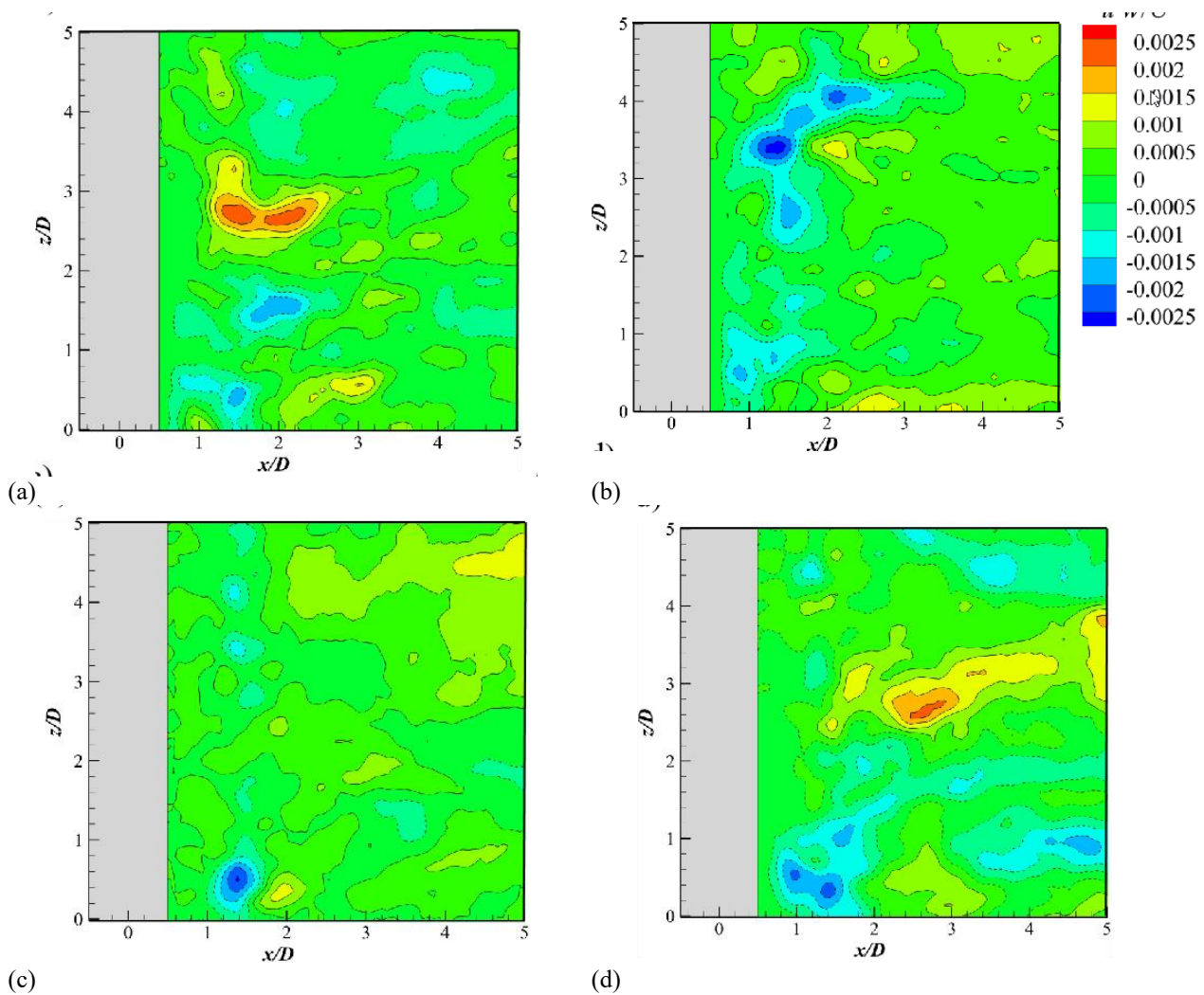


Fig. 21 Contours of the Reynolds stress $\overline{u'w'}/U^2$ in the (x, z) -plane at $y/D=0$. (a) smooth cylinder, (b) asymmetrically grooved cylinder with 4 grooves, (c) asymmetrically grooved cylinder with 12 grooves, (d) asymmetrically grooved cylinder with 24 grooves

Table 5 The maximum Reynolds Stress of asymmetric groove cylinders with different numbers of grooves

Number of asymmetric grooves	plain (x, y)		plain (x, z)	
	value	Deviation/%	value	Deviation/%
0	0.02	—	0.0023	—
4	0.011	-45.00	0.0013	-43.47
12	0.014	-30.00	0.0015	-34.78
24	0.018	-10.00	0.002	-13.04

respectively. Table 5 presents a comparison of the maximum Reynolds stress of the asymmetrically grooved cylinders. These cylinders have slightly lower maximum Reynolds stresses than the smooth cylinder, particularly the four-grooved one. This outcome may be attributed to the effect of the asymmetrically grooved structure on flow characteristics. The findings align with the conclusion of the Reynolds stress in the (x, y) plane.

4.5 Turbulent Kinetic Energy

The TKE is a physical quantity that describes the magnitude of the velocity fluctuations of a fluid mass. Figure 22 shows the normalized TKE profile of the smooth cylinder and asymmetrically grooved cylinders in the (x, y) plane. As shown in Fig. 22, the maximum turbulence

energy of the smooth cylinder is 0.084, whereas the values are approximately 0.05, 0.059 and 0.083 for cylinders with different numbers of asymmetric grooves. Table 6 presents a comparison of the maximum TKE of the asymmetrically grooved cylinders. The TKE of these cylinders could be reduced by 40.47%, 29.76%, and 1.19%, respectively, in comparison with that of the smooth cylinder. For the smooth cylinder, the TKE is highest at the cylinder tail, indicating the highest speed fluctuations in this section.

More energy is transferred from the mainstream region to the tail section, resulting in an increase in the velocity and dynamic pressure in the wake region (Qian, 2018). The maximum TKE value in the wake region of the cylinders with different numbers of asymmetrically

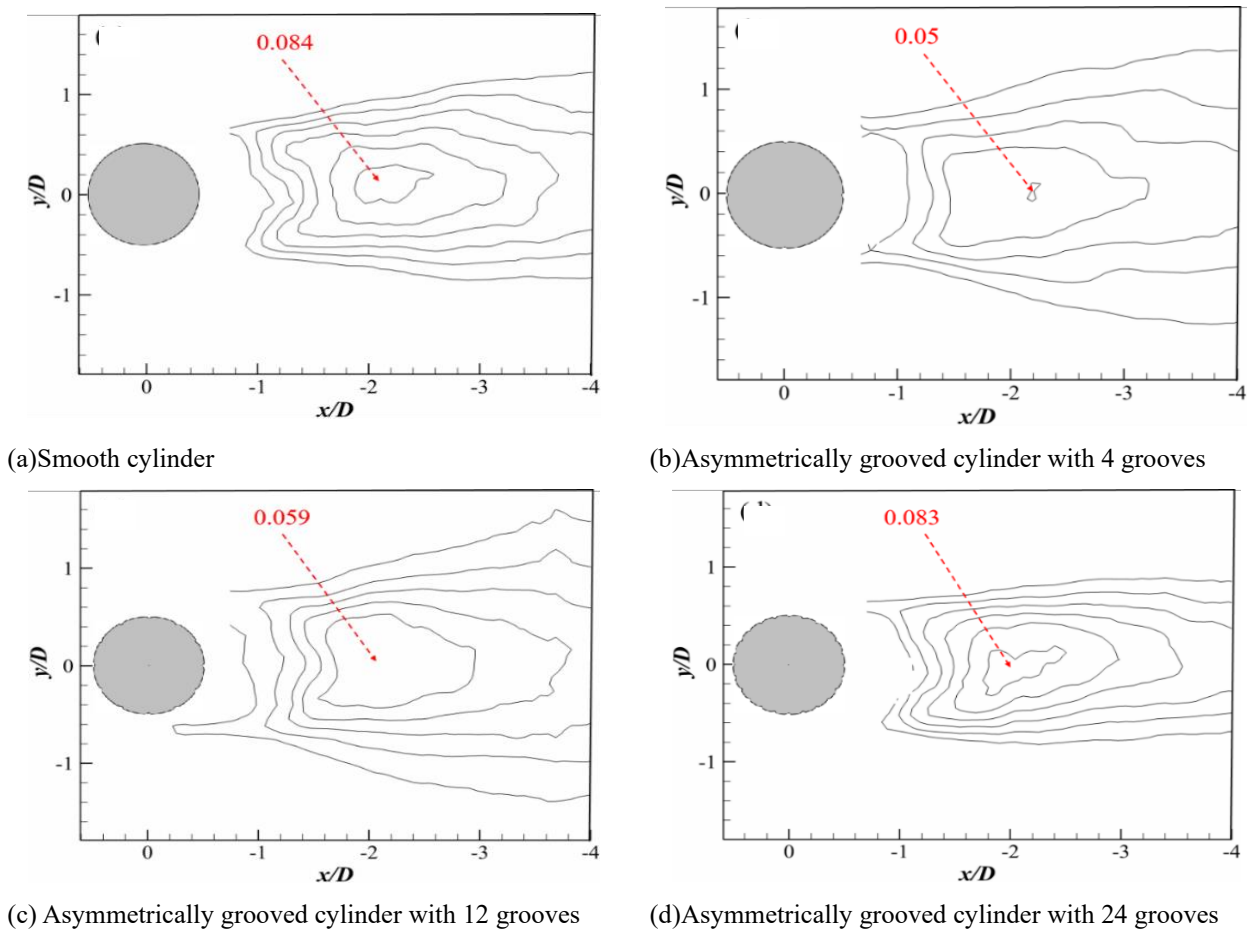


Fig. 22 Contours of the normalized turbulent kinetic energy in the (x, y) -plane at $z/D=0$

Table 6 The maximum TKE of asymmetric groove cylinders with different numbers of grooves

Number of asymmetric grooves	plain (x, y)		plain (x, z)	
	value	Deviation/%	value	Deviation/%
0	0.084	—	0.021	—
4	0.05	-40.47	0.015	-28.57
12	0.059	-29.76	0.016	-23.80
24	0.083	-1.19	0.018	-14.28

grooved structures was lower compared with that in the wake region of the smooth cylinder. This suggests that the asymmetrically grooved structures can suppress the velocity variation in the wake. In addition, the four-grooved asymmetric notched cylinder exhibited the lowest highest TKE. This can be attributed to the fact that the separation point of the asymmetrically grooved structure is closer to the downstream at this specific number, resulting in smaller vortices within the structure that restrict the formation of larger eddies.

Figure 23 presents the standardized distributions of the TKE in the spreading direction of the smooth cylinder and asymmetrically grooved cylinders. The maximum TKE of the smooth cylinder was found to be 0.021, whereas the maximum values for the asymmetrically grooved cylinders were approximately 0.015, 0.016, and 0.018. After varying the numbers of asymmetric groove cylinders, the maximum TKE values were slightly lower than that for the smooth cylinder. Because the asymmetrically grooved

structure can limit energy transfer from the main flow zone to the wake region and help control velocity variations in the wake region, the asymmetrically grooved structure can lower the energy (Zhou et al., 2015). In addition, the four-grooved asymmetric cylinder exhibited the lowest maximum TKE. This is a result of the separation point of the asymmetrically grooved structure being closer to the downstream at this particular number, which interferes more with the development of large eddies due to the small vortices present within the asymmetrically grooved structure. This is consistent with the conclusion that the TKE in the plane (x, y) . In addition, the finding that an increase in the number of grooves leads to an increase in the TKE confirms the simulation results (Qi, 2020). Specifically, the cylinder with grooves covering the entire surface exhibited a higher maximum TKE value within the wake region, a wider TKE region at the wake, and a lower drag reduction effect than that of the cylinder with grooves covering only half the surface.

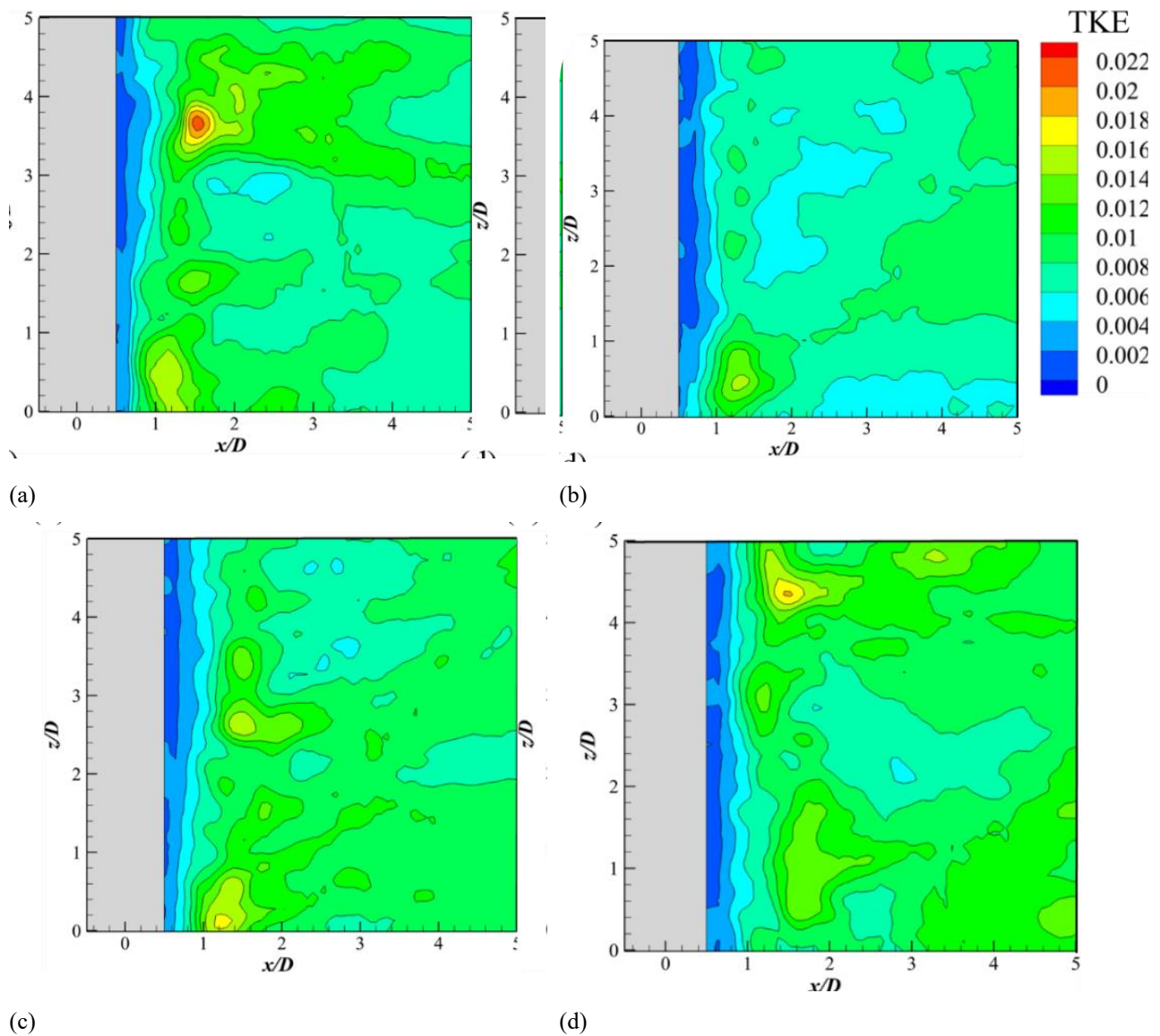


Fig. 23 Contours of the turbulent kinetic energy in the (x, z) -plane at $y/D=0$. (a) smooth cylinder, (b) asymmetrically grooved cylinder with 4 grooves, (c) asymmetrically grooved cylinder with 12 grooves, (d) asymmetrically grooved cylinder with 24 grooves

5. CONCLUSIONS

In this study, numerical simulation and experimental analysis were conducted to investigate the drag reduction properties of cylindrical winding flow over asymmetric grooves and the effect of the number of grooves on such characteristics. The following conclusions can be drawn from the simulation and experimental results:

(1) Both the simulation and experimental results showed a consistent trend: the presence of asymmetric grooves significantly improved the cylindrical flow performance, with the degree of improvement reducing with more number of grooves. The flow performance was optimal in the cylinder with four grooves, as confirmed by both simulation and experimental data. The use of four asymmetrical grooves reduced the dominant frequency of vortex shedding by 13.56% in the simulation and 14.42% in the experiment compared with that of the smooth cylinder, with a mere 0.7% difference between these

reductions. This confirmed the reliability of the experiments and simulations.

(2) Boundary layer separation is a key factor determining the characteristics of cylindrical winding flow. Our analysis indicated that a groove structure could delay the separation point, altering the flow at the tail, reducing the pressure differential between the front and back, and decreasing the winding flow resistance. Moreover, the position of flow breakdown and vortex on the fluid surface is delayed. The pressure differential perpendicular to the incoming velocity component significantly decreases, resulting in a lower lift coefficient amplitude during periodic vibration.

(3) A data analysis revealed optimal flow performance enhancement in the four-groove configuration. Increasing the number of grooves beyond this point led to diminished enhancement. This is because adding bionic groove units near the separation point facilitates momentum exchange between the fluid and the wall, preventing flow separation.

However, at high fluid turbulence levels near the separation point, adding more grooves can cause extreme turbulence, leading to premature flow separation.

ACKNOWLEDGMENTS

The author wishes to acknowledge the support given to him by the Natural Science Foundation of Jiangsu Province of China (No.BK20191459).

CONFLICT OF INTEREST

The authors declare that they have no competing interests.

AUTHORS CONTRIBUTION

Fei Yan: Conceptualization, methodology, data collection, resources. **Weiyu Kong:** conceptualization, formal-analysis, writing and editing the original draft, manuscript revision. **Huifeng Jiao:** data-curation, investigation. **Fei Peng:** validation, visualization. **Jian Zhang:** project-administration, funding-acquisition.

REFERENCES

- Becheffar, Y., & Chaib, K. (2023). The fluid flow characteristics around a triangular grooved cylinder. *International Journal of Modern Physics C*, 2350137. <https://doi.org/10.1142/S0129183123501371>
- Cao, Y., & Tamura, T. (2015). Numerical investigations into effects of three-dimensional wake patterns on unsteady aerodynamic characteristics of a circular cylinder at $Re=1.3 \times 10^5$. *Fluids Struct.* 59, 351–369. <https://doi.org/10.1016/j.jfluidstructs.2015.10.001>
- Chen, P., Sun, J., Cheng, Y. T., & Chen, W. Y. (2023). Experimental study on the flow pattern of double-hemisphere rough elements with different streamwise spacing. *Journal of Applied Fluid Mechanics*, 16(8), 1531-1543. <https://doi.org/10.47176/JAFM.16.08.1635>
- Li, W., Peng, S., & Xi, H. (2022). Experimental investigation on the degradation of turbulent friction drag reduction over semi-circular riblets. *Experiments in Fluids*, 63(12), 1-14. <https://doi.org/10.1007/s00348-022-03534-2>
- Menter, F., Kuntz, M., & Langtry, R. (2003). Ten years of experience with the SST Turbulence model. *Turbulence, Heat and Mass Transfer*, 4(1), 625-632. <https://doi.org/10.1016/j.tmm.2003.09.012>
- Parsons, D. R., Walker, I. J., & Wiggs, G. (2004). Numerical modelling of flow structures over idealized transverse aeolian dunes of varying geometry. Joint Meeting of the 5th International Conference on Aeolian. <https://doi.org/10.1016/j.geomorph.2003.09.012>
- Priyadarsan, A., & Afzal, M. S. (2023). Numerical investigation of flow past a circular cylinder modified with a single groove at low Reynolds number. *Physics of Fluids*, 35(2). <https://doi.org/10.1063/5.0137530>
- Qi, Y. (2020). *Research and application of bionic non-smooth surface cylindrical winding characteristics* [D, Zhejiang University].
- Qian, Q. (2018). *Study on drag reduction performance of water-conveying pipe on typical trench surface* [D, Southwest Petroleum University]. Chengdu.
- Rinoshika, H., & Rinoshika, A. (2019). Passive control of a front inclined hole on flow structures around a surface-mounted short cylinder. *Ocean Engineering*, 189(5), 106383. <https://doi.org/10.1016/j.oceaneng.2019.106383>
- Schewe, G. (1983). On the force fluctuations acting on a circular cylinder in crossflow from subcritical up to transcritical Reynolds numbers. *Journal of Fluid Mechanics*, 133, 265-285. <https://doi.org/10.1017/S0022112083001913>
- Soyler, M., Ozalp, C., & Polat, C. (2022). Experimental and numerical investigation of flow structure of grooved cylinder. *Ocean Engineering*, 264, 112478. <https://doi.org/10.1016/j.oceaneng.2022.112478>
- Tonui, N., & Sumner, D. (2009). *Temporal development of the wake of a non-impulsively started circular cylinder*. Asme Fluids Engineering Division Summer Meeting. <https://doi.org/10.1115/FEDSM2009-78018>
- Wang, H. F., & Zhou, Y. (2009). The finite-length square cylinder near wake. *Journal of Fluid Mechanics*, 638, 453-490. <https://doi.org/10.1017/S0022112009990693>
- Wang, L., Wang, C., & Wang, S. (2021). Design and analysis of micro-nano scale nested-grooved surface structure for drag reduction based on ‘Vortex-Driven Design. *European Journal of Mechanics-B/Fluids*, 85, 335-350. <https://doi.org/10.1016/j.euromechflu.2020.10.007>
- Yu, J. (2010). *PIV Experimental Study on the Flow around Cylindrical Cactus-like Structures* [D, Shanghai Jiao Tong University]. Shanghai.
- Zdravkovich, M. M. (1981). Review and classification of various aerodynamic and hydrodynamic means for suppressing vortex shedding. *Journal of Wind Engineering and Industrial Aerodynamics*, 7, 145-189. [https://doi.org/10.1016/0167-6105\(81\)90036-2](https://doi.org/10.1016/0167-6105(81)90036-2)
- Zhang, J., Ma, C., & Liu, J. (2022a). Experimental and numerical investigation of flow over spiral grooved cylinders. *Advances in Mechanical Engineering*, 14(8), 16878132221117350. <https://doi.org/10.1177/16878132221117350>
- Zhang, K., Ma, C., Zhang, J., Zhang, B., & Zhao, B. (2022b). Drag reduction characteristics of bionic structure composed of grooves and mucous membrane acting on turbulent boundary layer. *Journal of Applied Fluid Mechanics*, 15(1), 283-292. <https://doi.org/10.47176/JAFM.15.01.32901>
- Zheng, C., Zhou, P., & Zhong, S. (2023). On the cylinder

noise and drag reductions in different Reynolds number ranges using surface pattern fabrics. *Physics of Fluids*, 35(3), 035111. <https://doi.org/10.1063/5.0138074>

Zhou, B., Wang, X., Guo, W., Gho, W. M., & Tan, S. K. (2015). Experimental study on flow past a circular cylinder with rough surface. *Ocean Engineering*,

109(3),

7-13.

<https://doi.org/10.1016/j.oceaneng.2015.08.062>

Zou, L. (2008). Large-eddy simulation of flow around cylinder arrays at a subcritical Reynolds number. *Journal of Hydrodynamics*, 20(4), 403-413. [https://doi.org/10.1016/S1001-6058\(08\)60074-8](https://doi.org/10.1016/S1001-6058(08)60074-8)